Origami-driven Dzyaloshinskii-Moriya interaction in centrosymmetric two-dimensional magnets

Jiawei Jiang,[1] Yonglong Ga,[2] Peng Li,[2] Qirui Cui,[2] Liming Wang,[1] Dongxing Yu,[2] Jinghua Liang,[2] and Hongxin Yang[1,2,*]

[1]*National Laboratory of Solid State Microstructures, School of Physics, Collaborative Innovation Center of Advanced Microstructures, Nanjing University, Nanjing 210093, China*

[2]*Ningbo Institute of Materials Technology and Engineering, Chinese Academy of Sciences, Ningbo 315201, China*

(Received 26 July 2023; revised 25 October 2023; accepted 8 December 2023; published 3 January 2024)

Origami-inspired approaches have presented exciting possibilities for engineering and manipulating two-dimensional (2D) materials in three-dimensional space. By introducing curvature through folding and bending, curved 2D materials offer unique opportunities to explore exotic magnetic phenomena that are absent in their planar counterparts. Here we demonstrate the existence of origami-driven Dzyaloshinskii-Moriya interaction (DMI) in centrosymmetric 2D magnets by means of symmetry analysis and noncollinear spin-polarized density functional theory. By taking CrI_3 as an example, we show the decisive effect of spin-orbit interaction on the DMI of folded structures, which corresponds to the three-site Fert-Lévy model. Furthermore, the geometry-governed anisotropy and the DMI contribute to the magnetic energy, resulting in chiral domain walls as the ground state. Our results present a general method for creating topological spin textures in centrosymmetric 2D magnets, providing insights into the formation of magnetochirality in origami 2D magnets, which will be beneficial to both the fundamental study of curvilinear magnetism and the application of chiral spin textures in spintronic devices.

DOI: 10.1103/PhysRevB.109.014402

I. INTRODUCTION

Origami-inspired synthesis methods and curvature-induced unconventional magnetic effects have triggered a general trend to extend planar two-dimensional (2D) magnetic structures into three-dimensional space in recent years [1–7]. Diverging from planar systems, the presence of curvature in a system can introduce additional effective energy contributions, i.e., scalar and vector geometrical potentials [1,8]. As a consequence, this approach provides the means to launch novel functionalities by modulating the local curvature of the geometry, resulting in several magnetochiral effects and topological magnetization patterns, such as increased domain wall velocities [9] and chirality symmetry breaking [10–14].

In systems with symmetry breaking, the antisymmetric Dzyaloshinskii-Moriya interaction (DMI) can modify the conventional long-range magnetic order and hence induce the formation of topological magnetism [15–24]. This phenomenon has been achieved in diverse systems, spanning chiral magnets [25–30], interfaces [31–42], and 2D materials [43–49]. Remarkably, micromagnetic simulations have demonstrated the emergence of topological magnetization patterns in magnets with curved geometry, highlighting instances where the presence of DMI is not necessary [1,50–52]. Nevertheless, existing micromagnetic models have certain limitations as they only treat the anisotropy and DMI as nonrelativistic effects by a coordinate transformation, ignoring the influence of spin-orbit coupling (SOC) on the above terms in curvature-dependent geometry. In this context, density functional theory (DFT) helps one to understand the emerging properties of magnets under specific geometries and provides precise material parameters [8,42,48], albeit with the constraint of periodic boundary conditions requiring a supercell with numerous atoms. For the term of material selection, 2D magnets with intrinsic long-range magnetic order are particularly well suited for investigating magnetochiral effects, aided by their flexibility in origami 2D structures and natural occurrence of ripples and folds [53–57].

Here, we perform a symmetry analysis, noncollinear spin-polarized DFT calculation, and atomic spin simulation to investigate the magnetic properties and topological magnetization patterns in folded centrosymmetric 2D magnets with local curvature. Using CrI_3 as an example, we discover that fully SOC-mediated DMI can be induced in folded systems, with the magnitude of DMI depending on the curvature. The curvature-dependent anisotropy and DMI result in the emergence of magnetochiral effects, such as the chiral domain walls in folded CrI_3. Moreover, the conclusions drawn from folded CrI_3 can be generalized to a variety of 2D magnets with centrosymmetry. In contrast to existing models and studies, our results underscore the pivotal role of SOC in generating DMI in curved geometries. We also propose a general approach for introducing origami-driven topological spin textures in centrosymmetric 2D magnets. These findings not only advance the fundamental understanding of curvilinear magnetism but also establish a robust physical foundation for future applications involving topological spin textures in 2D origami magnets.

II. GEOMETRIC MODEL

Here we consider a 2D origami structure consisting of two rigid parts and a curved hinge part with a box-function

*Corresponding author: hongxin.yang@nju.edu.cn

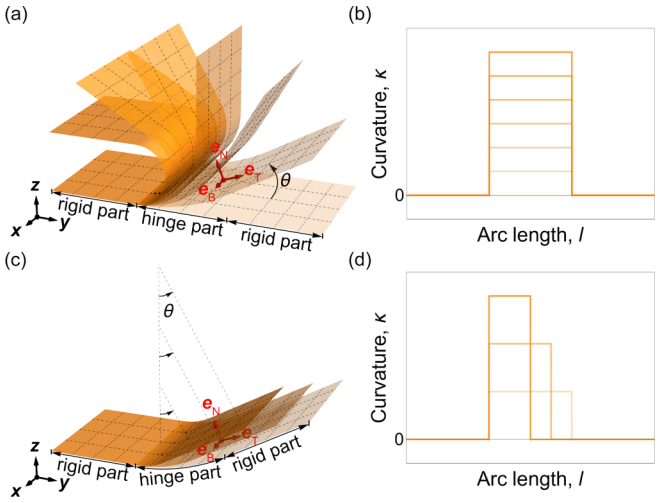

FIG. 1. (a) Folding of 2D magnets characterized by the folding angle θ. (b) Box-function spatial profile of curvature for the folded systems with folding angle θ. (c) Folding of 2D magnets characterized by the hinge length l. (d) Box-function spatial profile of curvature for the folded systems with hinge length l.

curvature profile: $\kappa(l) = \kappa_0 H(l + l_0) - \kappa_0 H(l - l_0)$, where $H(x)$ is the Heaviside step function and κ_0 is the curvature of the hinge part with the arc length l_0. Specifically, we consider a nonchiral folded structure where the projection of the structure onto the yz plane forms a one-dimensional nanowire with an individual circular segment. Furthermore, the curvature of the hinge part can be expressed as $\kappa = \theta/l$ to construct an (N,θ) folded system with folding angle θ, lattice constant a, and hinge length l composed of N units of the cell in the folding direction. Adjusting the folding angle influences the shape and curvature distribution of the folded structures, while varying the length of the hinge part can result in different bending patterns and curvatures, as illustrated in Fig. 1. This control over the geometric parameters enables the manipulation of the folded structure's overall curvature, thereby exerting control over its magnetic properties.

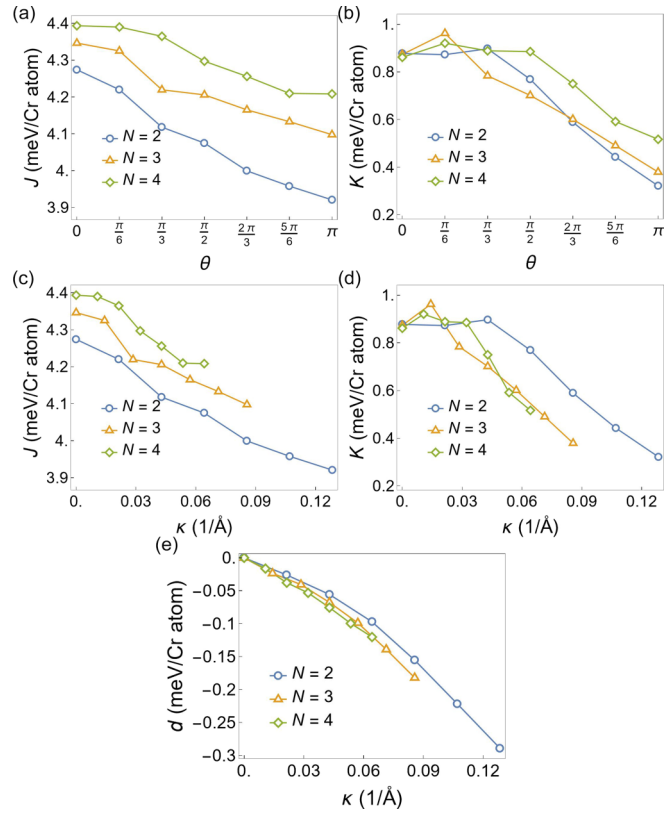

FIG. 3. Calculated magnetic parameters of folded CrI_3. (a) J as a function of θ. (b) K as a function of θ. (c) J as a function of κ. (d) K as a function of κ. (e) d as a function of κ.

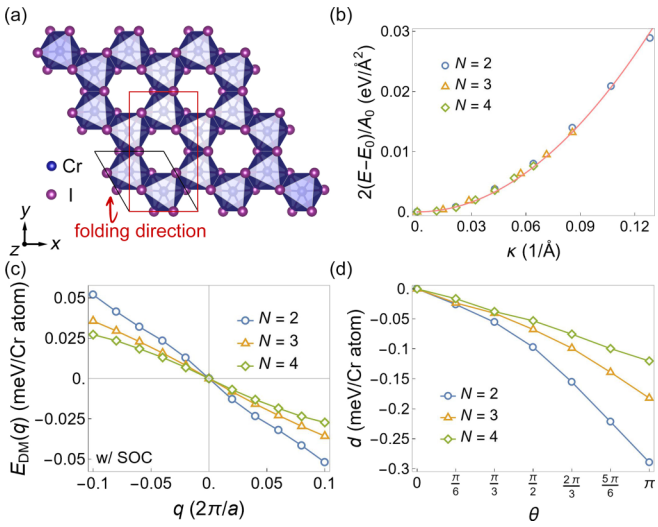

FIG. 2. (a) Armchair folding configuration of CrI_3. The primitive and rectangle units are shown in the black and red frames. (b) Total energy per unit area of folded CrI_3 as a function of curvature κ. (c) DMI energy of $(N,\pi/2)$ folded CrI_3 as a function of spin spiral vector $\boldsymbol{q}$ when SOC is included. (d) DMI parameter d of (N,θ) folded CrI_3.

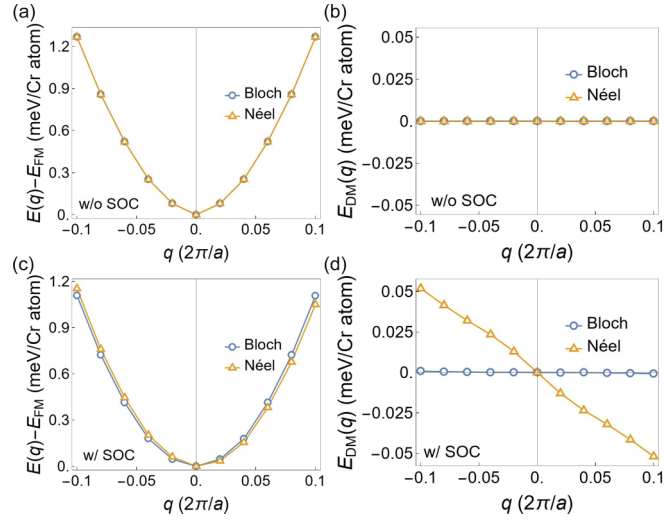

FIG. 4. (a) Total energy of spin spiral and (b) DMI energy of $(2,\pi/2)$ folded CrI_3 as a function of spin spiral vector $\boldsymbol{q}$ when SOC is excluded. (c) Total energy of spin spiral and (d) DMI energy of $(2,\pi/2)$ folded CrI_3 as a function of spin spiral vector $\boldsymbol{q}$ when SOC is included.

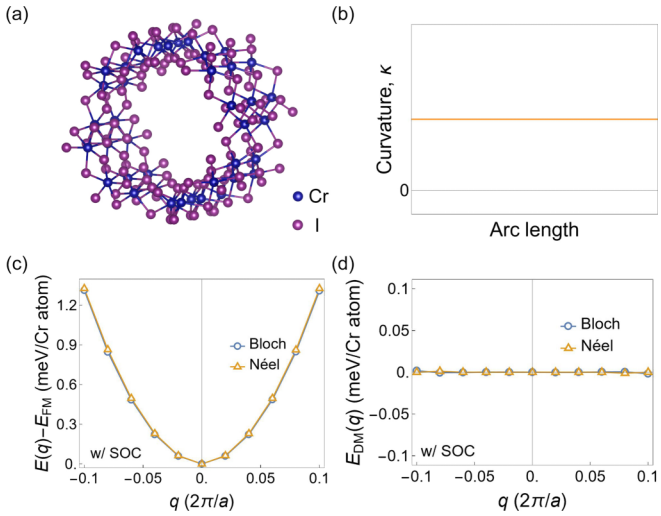

FIG. 5. (a) Structure of CrI_3 nanotube with $N = 4$. (b) Constant curvature for the nanotube systems. (c) Total energy of spin spiral and (d) DMI energy of CrI_3 nanotube with $N = 4$ as a function of spin spiral vector $\boldsymbol{q}$ when SOC is included.

III. SYMMETRY ANALYSIS

To provide clarification, the second-order DMI tensor for crystallographic point groups can be derived by applying the Neumann principle of crystallography and generating matrices [58,59], which is expressed as

$$D_{ij} = |\sigma|\sigma_{ii'}\sigma_{jj'}D_{i'j'}, \tag{1}$$

with σ being all the symmetry operations contained in the specific point group. The nonzero entries in the matrix determine the type of DMI, i.e., Néel, Bloch, or mixed. We then analyze the symmetry of the folded centrosymmetric 2D magnets by taking monolayer CrI_3 as an example, which attracted tremendous attention as one of the first-reported 2D magnets with intrinsic ferromagnetism [54,60,61]. Flat CrI_3 has a D_{3d} point-group symmetry, which includes an inversion operation that disallows the existence of the DMI term. In the case of folded CrI_3, the presence of folding results in the loss of inversion and rotational symmetry, leading to a reduced point-group symmetry of C_s containing two symmetry operations of an identity operation and a mirror reflection. With Eq. (1), we can identify the DMI tensor of the C_s point group:

$$D(C_s) = \begin{pmatrix} 0 & 0 & D_{13} \\ 0 & 0 & D_{23} \\ D_{31} & D_{32} & 0 \end{pmatrix} \tag{2}$$

with four independent nonzero off-diagonal entries D_{13}, D_{23}, D_{31}, and D_{32}. This essentially ensures the existence of a Néel-type DMI in folded CrI_3, while a Bloch-type DMI is absent under this condition.

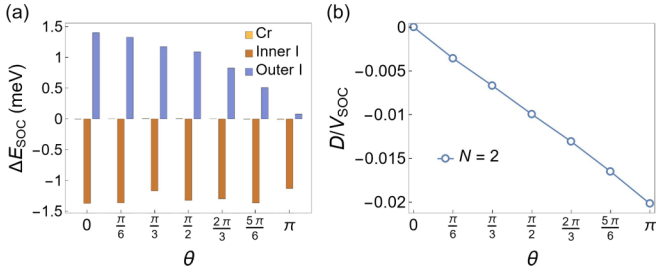

FIG. 6. (a) Calculated SOC energy difference ΔE_{SOC} associated with DMI and (b) DMI parameter D/V_{SOC} using Fert-Lévy model of $(2,\theta)$ folded CrI_3.

IV. MAGNETISM IN FOLDED CrI_3

Here we show the geometry-governed magnetism in folded CrI_3 by DFT. As shown in Fig. 2(a), we consider the armchair folding configuration to construct (N,θ) folded CrI_3 for $N = 2,3,4$ and $\theta = \pi/6, \pi/3, \pi/2, 2\pi/3, 5\pi/6, \pi$. Both rigid parts contain one rectangle unit of flat CrI_3, which has been tested to ensure the accuracy of the magnetic energy (see Appendix A). The total energies per unit area of the relaxed (N,θ) folded CrI_3 with a collinear ferromagnetic state in a spin-polarized calculation are plotted in Fig. 2(b). The bending moduli of CrI_3, determined by $2(E - E_0)/A_0 = \alpha\kappa^2$ with E_0 and A_0 being the total energy and surface area of the flat unit, is fitted to be $\alpha = 1.81$ eV, which is close to monolayer graphene and transition metal dichalcogenides [62].

For the folded structures, we adopt the curvilinear spin Hamiltonian, which contains Heisenberg exchange J, Dzyaloshinskii-Moriya term $\boldsymbol{D}$, and magnetic anisotropy K, which is expressed as

$$\mathcal{H} = -\sum_{\langle i,j\rangle} J_{ij}\boldsymbol{S}_i \cdot \boldsymbol{S}_j - \sum_{\langle i,j\rangle} \boldsymbol{D}_{ij} \cdot (\boldsymbol{S}_i \times \boldsymbol{S}_j) - \sum_{\langle i\rangle} K_i \left(S_i^{\boldsymbol{e}_{\mathrm{N}}}\right)^2, \tag{3}$$

which models the interaction of an atomic unit spin moment $\boldsymbol{S}$ at position $\boldsymbol{r}$. The discrete spin moment $|\boldsymbol{S}| = 1$ can be utilized by introducing the spherical angular parameter $\boldsymbol{S} = \sin\vartheta\,\sin\phi\boldsymbol{e}_{\mathrm{B}} + \sin\vartheta\,\cos\phi\boldsymbol{e}_{\mathrm{T}} + \cos\vartheta\boldsymbol{e}_{\mathrm{N}}$ with curvilinear basis $[\boldsymbol{e}_{\mathrm{B}}, \boldsymbol{e}_{\mathrm{T}}, \boldsymbol{e}_{\mathrm{N}}]$, where $\boldsymbol{e}_{\mathrm{N}}$ and $\boldsymbol{e}_{\mathrm{T}}$ are the unit vectors in normal and tangential directions, and $\boldsymbol{e}_{\mathrm{B}} = \boldsymbol{e}_{\mathrm{T}} \times \boldsymbol{e}_{\mathrm{N}}$ is the binormal unit vector. The Heisenberg exchange interaction is determined by the energy differences of collinear magnetic states, and the magnetic anisotropy is obtained by the calculation of magnetization along three curvilinear coordinate directions. For the (N,θ) folded CrI_3, the Heisenberg exchange and magnetic anisotropy terms both decrease with the increasing θ (see Fig. 3). Moreover, both of these terms are almost positively correlated with N. We also graph the calculated J and K values as functions of κ (see Fig. 3). J is enhanced with increasing N for the fixed curvature, while K is almost weakened with increasing N. The increase in curvature weakens the ferromagnetic coupling, thereby leading to a reduction in the long-range magnetic order according to the spin wave theory [63] and facilitating the emergence of spin textures.

To precisely determine the Dzyaloshinskii-Moriya parameter of the folded structure, we calculate the spin spiral energy dispersion $E(\boldsymbol{q})$ as a function of spin spiral wave vector $\boldsymbol{q}$, including SOC, and obtain the evolution of DMI energy with $\boldsymbol{q}$ (see Appendix A). For the Néel-type DMI, which is allowed in the folded structures as discussed, the Dzyaloshinskii-Moriya vector can be written as $\boldsymbol{D}_{ij} = d_{ij}(\boldsymbol{e}_{\mathrm{N}} \times \boldsymbol{u}_{ij})$ with $\boldsymbol{u}_{ij}$ being

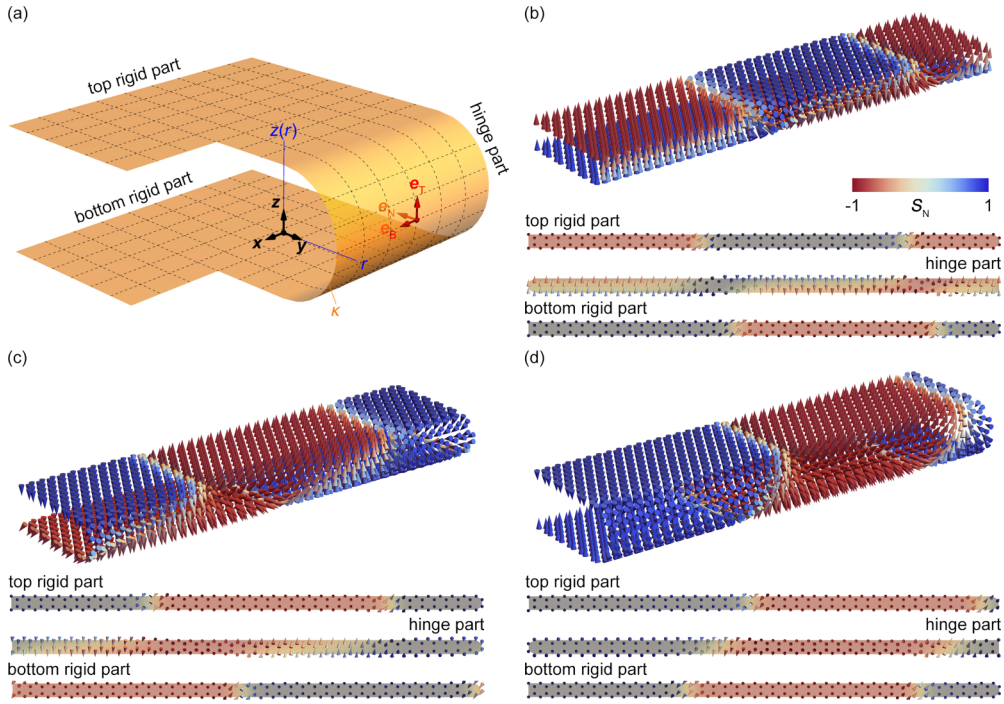

FIG. 7. (a) Sketch of the geometry with the Cartesian $[x, y, z]$ and curvilinear $[e_B, e_T, e_N]$ frames of folded systems. (b) Spin textures of $(2,\pi)$ folded CrI_3. (c) Spin textures of $(3,\pi)$ folded CrI_3. (d) Spin textures of $(4,\pi)$ folded CrI_3.

the unit vector pointing from r_i to r_j. In Fig. 2(c), we show the DMI energy $E_{DM}(q)$ of $(N,\pi/2)$ folded CrI_3 of various q within $|q| \leqslant 0.1(2\pi/a)$ with Néel-type planar spiral configuration. Here the positive and negative values of q correspond to the spin spirals of clockwise and anticlockwise chirality. For each system, the calculated data decreases linearly with the increase of q, indicating the existence of Néel-type DMI in the folded structures. Interestingly, the DMI energy shows a negative relationship with N, which is exactly the opposite of the trend for the Heisenberg exchange and magnetic anisotropy terms. Similarly, the DMI parameter d exhibits a smooth monotonic behavior with θ, showing that the DMI term is enhanced with increasing curvature, as plotted in Fig. 2(d). For a fixed curvature, the DMI energy is increased with increasing hinge length N (see Fig. 3). Further calculations show that the energy of Bloch-type DMI is inessential (see Fig. 4), which is consistent with the symmetry analysis. It is noteworthy that in the absence of SOC, the energy dispersion of the spin spiral exhibits degeneracy for $+q$ and $-q$, with both Bloch- and Néel-type spirals having the same energy. This result highlights the crucial role of spin-orbit interaction in the energy contribution of DMI in (N,θ) folded CrI_3. Moreover, SOC-meditated Néel-type DMI vanishes in $(N,2\pi)$ folded CrI_3, i.e., CrI_3 nanotube (see Fig. 5).

To further elucidate the variation mechanism of SOC-meditated DMI with curvature in folded structures, we calculate the SOC energy difference ΔE_{SOC} between opposite spin spirals of $(2,\theta)$ folded CrI_3, as shown in Fig. 6(a). We adopt the I atoms pointing towards the side of $\boldsymbol{e}_N$ as inner I atoms, and the I atoms on the other side as outer I atoms, with the Cr atoms at the center in folded CrI_3. It is clear that almost all ΔE_{SOC} stems from the adjacent I atoms, while contributions from Cr atoms can be ignored. With increasing θ, the opposite ΔE_{SOC} of inner and outer I atoms cannot offset each other, leading to an overall increase in the total DMI. The DMI effect of folded CrI_3 can also be modeled as the sum of each Cr-I-Cr trimer, which is corresponding to the three-site Fert-Lévy model [64], where the hopping of two spins of magnetic atoms can induce DMI through an adjacent nonmagnetic atom with a large SOC. The three-site Fert-Lévy model for antisymmetric DMI is expressed as

$$\boldsymbol{D}_{ijl}(\boldsymbol{r}_{li},\ \boldsymbol{r}_{lj}, \boldsymbol{r}_{ij}) = -V_{SOC}\frac{(\boldsymbol{r}_{li}\cdot\boldsymbol{r}_{lj})(\boldsymbol{r}_{li}\times\boldsymbol{r}_{lj})}{|\boldsymbol{r}_{li}|^3|\boldsymbol{r}_{lj}|^3|\boldsymbol{r}_{lj}|}. \quad (4)$$

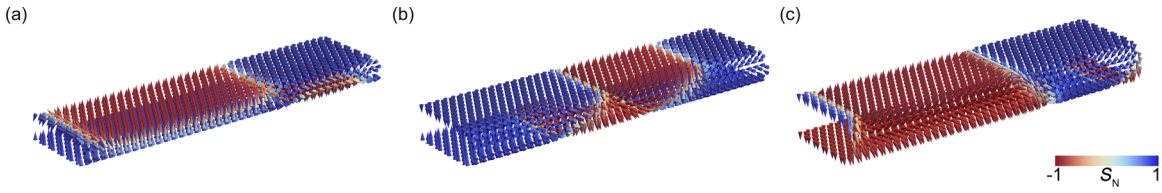

FIG. 8. Spin textures of (a) $(2,\pi)$, (b) $(3,\pi)$, and (c) $(4,\pi)$ folded CrI_3 when the spin Hamiltonian includes magnetostatic interactions.

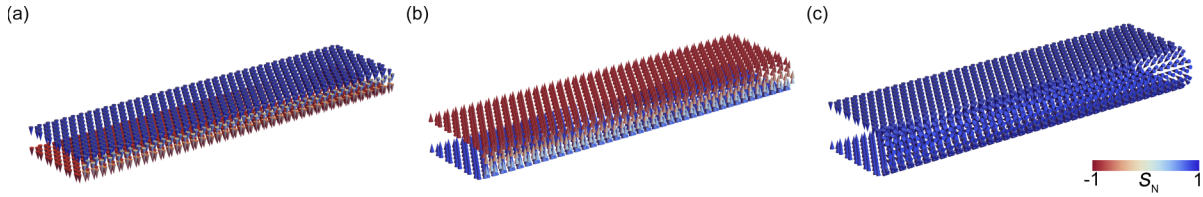

FIG. 9. Spin textures of (a) $(2,\pi)$, (b) $(3,\pi)$, and (c) $(4,\pi)$ folded CrI_3 when DMI is excluded.

Here V_{SOC} is a SOC-governed parameter written as $V_{SOC} = \frac{135\pi}{32}\frac{\lambda_d \Gamma^2}{k_F^3 E_F^2}\sin\frac{Z_d\pi}{10}$ with λ_d, Γ, k_F, E_F, and Z_d being the SOC constant, exchange interaction parameter between the localized spins and the spins of conduction electrons, Fermi vector, Fermi energy, and the number of d electrons [64]. In the frame of folded systems, we can further derive Eq. (4) as

$$\boldsymbol{D} = -V_{SOC}\sum_{\langle i,j\rangle}\frac{2\sin 2\varphi \sin^2\frac{\varphi}{2}\boldsymbol{e}_N}{r_{ij}}, \tag{5}$$

in which φ presents the bond angle of the Cr-I-Cr trimer. As the curvature increases, the difference between the $Cr-I_{inner}-Cr$ and $Cr-I_{outer}-Cr$ bond angles also increases. According to Eq. (5), this change in curvature is expected to result in a corresponding variation of the DMI's magnitude. In Fig. 6(b), we evaluate the DMI parameter of the $(2,\theta)$ folded CrI_3 as a function of the folding angle θ using the Fert-Lévy model, where we adopt V_{SOC} as a constant for a given folded system to qualitatively describe the dependence of DMI on curvature. For $(2,\theta)$ folded CrI_3, one can see that the DMI parameter monotonically increases with increasing curvature, which is in good agreement with the results from DFT calculations.

V. CHIRAL DOMAIN WALLS IN FOLDED CrI_3

To investigate the effect of SOC-meditated DMI on the static spin profiles in folded CrI_3, we perform spin dynamic simulation by solving an atomistic Landau-Lifshitz-Gilbert equation (see Appendix A). The effective magnetic field is modeled using a curvilinear spin Hamiltonian for each folded structure. The hinge part is modeled by the revolution of curvature $\kappa(r) = \kappa_0 r\boldsymbol{e}_y + \kappa_0 z(r)\boldsymbol{e}_z$ with the conversion of the geometry with the Cartesian $[x, y, z]$ to the curvilinear $[e_B, e_T, e_N]$ frames, as shown in Fig. 7(a). We consider the constant curvature in form $z(r) = \sqrt{1-r^2}$ to correspond to the geometry as mentioned. Figures 7(b)–7(d) display the relaxed spin textures of (N,π) folded CrI_3 with $N = 2$, 3, and 4 at 0 K, where all considered systems can hold chiral domain walls as a ground state. Interestingly, we find that the domain wall in the top and bottom rigid layers shifts due to the presence of the hinge part, and the displacement decreases with the increase of N. The chiral domain wall states are robust in the folded systems when the magnetostatic interactions are considered (see Fig. 8). We also adopt the curvilinear spin Hamiltonian excluding the Dzyaloshinskii-Moriya term (see Fig. 9). Both systems with $N = 2$ and 3 exhibit a complete ferromagnetic state, while a deformed ferromagnetic state with all spins pointing to $\boldsymbol{e}_N$ is formed in the $N = 4$ system, which originates from the competition between the Heisenberg exchange and the geometry-governed anisotropy. The present results highlight the contribution of DMI to the magnetic energy, leading to the nontrivial magnetochiral effects in folded structures. The phase transition temperatures at which chiral domain walls vanish are, respectively, 11.1, 15.5, and 9.5 K for the $N = 2$, 3, and 4 systems (see Fig. 10).

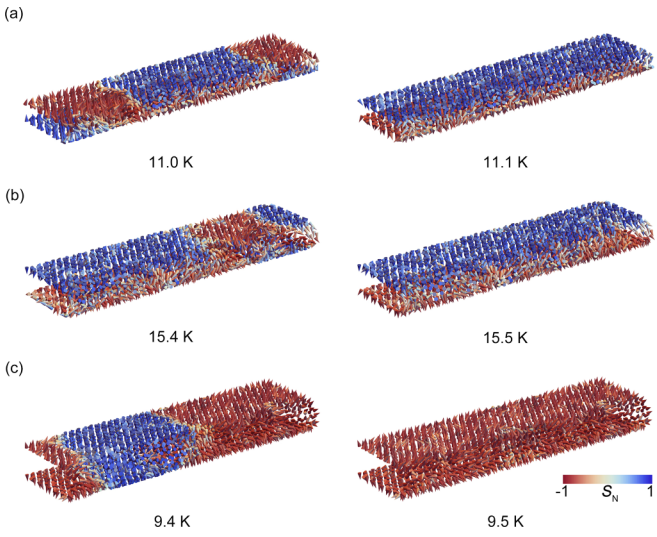

FIG. 10. Spin textures of (a) $(2,\pi)$, (b) $(3,\pi)$, and (c) $(4,\pi)$ folded CrI_3 near the magnetic phase transition temperature.

VI. CONCLUSION

We have performed symmetry analysis, noncollinear spin-polarized DFT, and atomistic spin simulation to investigate the curvature-induced DMI and corresponding magnetochiral effects in folded centrosymmetric CrI_3. The results demonstrate the influence of curvature effects on the DMI in folded CrI_3 when relativistic effect is considered. More importantly, our results show that the geometry-governed DMI in folded CrI_3 is completely mediated by spin-orbit interaction, which can be explained in the frame of the Fert-Lévy model, more profound than the previously understanding derived from the *ab initio* results [8,65]. The geometry-dependent anisotropy and DMI contribute to the formation of chiral domain walls as the ground state. Based on our developed curvilinear spin Hamiltonian and computational methods, these conclusions for CrI_3 can be generalized to a wider range of 2D magnets with inversion symmetry (see Fig. 11). Our work proposes a method by which the origami technique can introduce antisymmetric DMI and thereby topological spin textures in centrosymmetric 2D magnets, which holds promise for advancing the fundamental understanding of curvilinear magnetism and

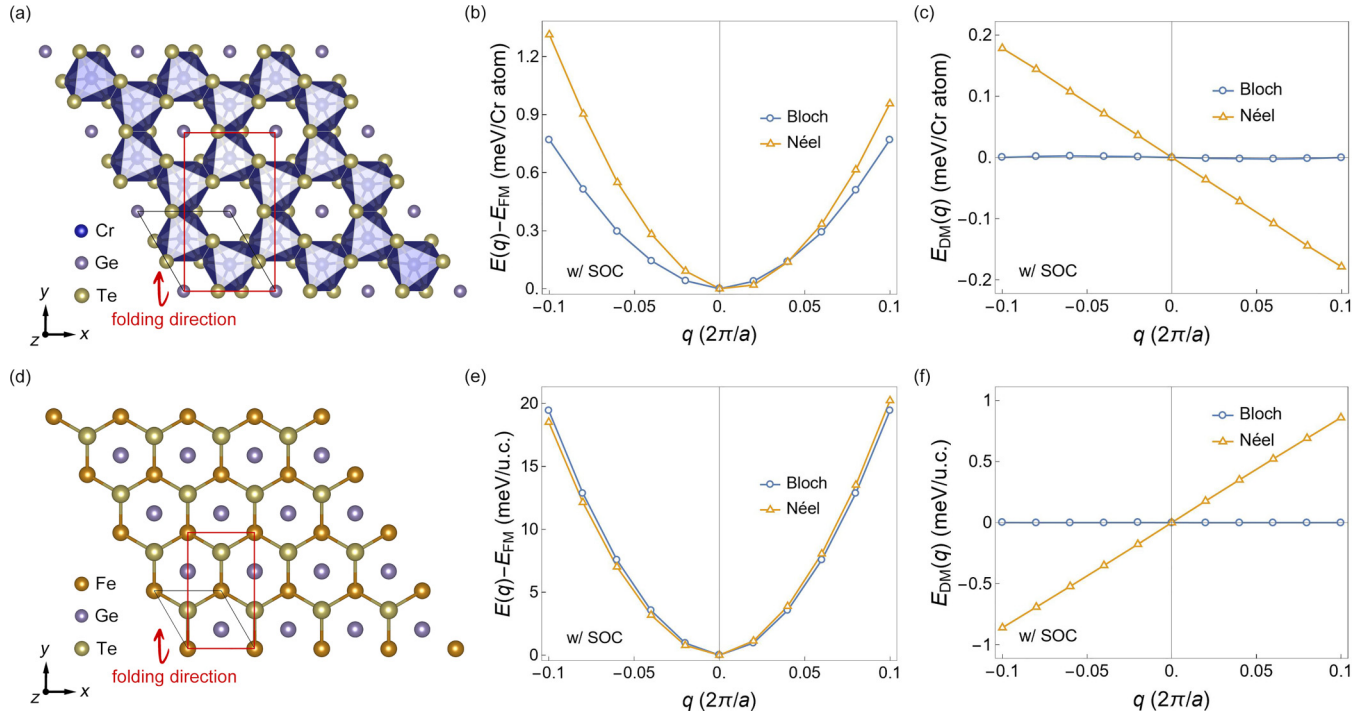

FIG. 11. (a) Armchair folding configuration of $CrGeTe_3$. (b) Total energy of spin spiral and (c) DMI energy of $(3,\pi)$ folded $CrGeTe_3$ as a function of spin spiral vector $\boldsymbol{q}$ when SOC is included. (d) Armchair folding configuration of Fe_3GeTe_2. (e) Total energy of spin spiral and (f) DMI energy of $(5,\pi)$ folded Fe_3GeTe_2 as a function of spin spiral vector $\boldsymbol{q}$ when SOC is included.

offers opportunities to design and explore exotic magnetic properties in 2D origami structures.

ACKNOWLEDGMENTS

This work was supported by the National Key Research and Development Program of China (MOST) (Grants No. 2022YFA1405100 and No. 2022YFA1403601), the "Pioneer" and "Leading Goose" R&D Program of Zhejiang Province (Grant No. 2022C01053), the National Natural Science Foundation of China (Grants No. 12174405 and No. 12204497), and Ningbo Key Scientific and Technological Project (Grant No. 2021000215).

APPENDIX A: CALCULATION METHODS

DFT calculations are performed with the projector augmented wave method as implemented in the Vienna *ab initio* simulation package [66–69]. The exchange correlation effects are treated by the generalized gradient approximation in the Perdew-Burke-Ernzerhof form [70]. The energy cutoff for plane wave expansion is 350 eV, and a $4\times1\times1$ Γ-centered k-point mesh for the Brillouin zone integration is used for the folded structures. Except for the magnetic atoms in the rigid part, the remaining atoms in the folded structures are fully relaxed with collinear ferromagnetic states until the Hellmann-Feynman force acting on each atom is less than 3 meV/Å. The energy convergence criterion is set to 10^{-7} eV to ensure the accuracy of magnetic interaction calculations. Both rigid parts contain one rectangle unit of flat CrI_3. Using two rectangle units of flat CrI_3 in rigid parts changes the DMI parameter d less than 7%. The I atom is set to be the termination in both rigid parts, which results in $4N+8$ Cr atoms and $12N+26$ I atoms in the (N,θ) folded CrI_3. A vacuum region of about 15 Å is added in both y and z directions to prevent the artificial coupling between the adjacent periodic images. Partly occupied $3d$ orbitals of Cr atoms are treated using an additional Coulomb repulsion [71] of $U = 2.65$ eV [72].

To determine the Heisenberg term of the folded systems, we first focus on the flat CrI_3 monolayer. Four magnetic states, i.e., ferromagnetic (FM), Néel-type antiferromagnetic (AFM), stripe-type AFM, and zigzag-type AFM states are considered, as shown in Fig. 12. A $2\times1\times1$ supercell and an $8\times16\times1$ k-point mesh are used in the calculations. The DFT energy of

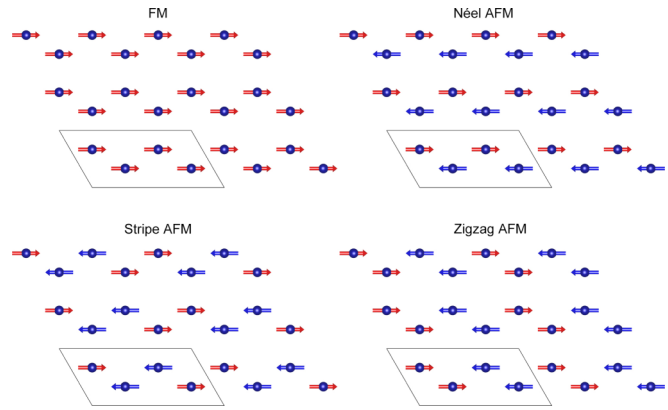

FIG. 12. Four magnetic states to calculate J_1–J_3 of flat CrI_3.

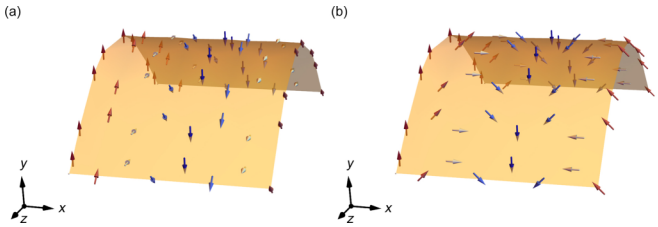

FIG. 13. Schematic of (a) Bloch- and (b) Néel-type spin spiral used to calculate the DMI. The spin spiral wave vector $\boldsymbol{q}$ is along the x axis.

each magnetic state can be written as

$$\begin{aligned} E_{\mathrm{FM}} &= E_0 - 12J_1 - 24J_2 - 12J_3, \\ E_{\mathrm{Néel\,AFM}} &= E_0 + 12J_1 - 24J_2 + 12J_3, \\ E_{\mathrm{stripe\ AFM}} &= E_0 - 4J_1 + 8J_2 + 12J_3, \\ E_{\mathrm{zigzag\ AFM}} &= E_0 + 4J_1 + 8J_2 - 12J_3. \end{aligned} \tag{A1}$$

Here E_0 is the energy independent of spin. The calculated J_{ij} is $J_1 = 4.40$ meV, $J_2 = 0.72$ meV, and $J_3 = -0.30\mu$eV, indicating that the nearest neighbor shell contributes most to the Heisenberg exchange interaction. Thus, for the folded systems, we compare the energy difference between the FM and Néel AFM states to obtain the equivalent nearest neighbor J. For the term of Dzyaloshinskii-Moriya, we perform the qSO method to calculate the spin spiral energy dispersion in the reciprocal space via generalized Bloch theorem and treat SOC in a self-consistent way within the frame of first-order perturbation theory [73,74]. We consider a Néel-type planar spiral configuration for the (N,θ) folded structures with the rotation axis $\boldsymbol{R} = (0, \cos\frac{\theta}{2}, \sin\frac{\theta}{2})$, where the spin moment $\boldsymbol{S}_i$ at position $\boldsymbol{r}_i$ reads

$$\boldsymbol{S}_i = \left[\cos(\boldsymbol{q}\cdot\boldsymbol{r}_i), -\sin(\boldsymbol{q}\cdot\boldsymbol{r}_i)\sin\frac{\theta}{2}, \sin(\boldsymbol{q}\cdot\boldsymbol{r}_i)\cos\frac{\theta}{2}\right] \tag{A2}$$

characterized by a spiral wave vector $\boldsymbol{q} = (q, 0, 0)$ perpendicular to $\boldsymbol{R}$, as shown in Fig. 13. Since the curvature of the hinge part is constant in our model, we adopt the DMI parameter d of the same size for each magnetic atom in the hinge part due to the box-function curvature profile. Thus, the normal vector $\boldsymbol{e}_{\mathrm{N}}$ in the Dzyaloshinskii-Moriya vector $\boldsymbol{D}_{ij} = d_{ij}(\boldsymbol{e}_{\mathrm{N}} \times \boldsymbol{u}_{ij})$ for the considered spin spiral can be simplified as $\boldsymbol{e}_{\mathrm{N}} = (0, -\sin\frac{\theta}{2}, \cos\frac{\theta}{2})$. Then the DMI energy can be written as

$$E_{\mathrm{DM}}(\boldsymbol{q}) = \sum_{\langle i,j\rangle} d_{ij}^{y} \sin(\boldsymbol{q}\cdot\boldsymbol{r}_{ij}). \tag{A3}$$

To extract the DMI contribution from total magnetic energy, the DMI energy can be further expressed by

$$\Delta E_{\mathrm{DM}}(\boldsymbol{q}) = \frac{E_{\mathrm{DM}}(\boldsymbol{q}) - E_{\mathrm{DM}}(-\boldsymbol{q})}{2} = \sum_{\langle i,j\rangle} d_{ij}^{y} \sin(\boldsymbol{q}\cdot\boldsymbol{r}_{ij}). \tag{A4}$$

For the honeycomb magnetic lattice, such as CrI_3, the DMI energy is derived as

$$\Delta E_{\mathrm{DM}}(\boldsymbol{q}) = \sqrt{3}d \sin\left(\frac{qa}{2}\right), \tag{A5}$$

where a is the lattice constant. For spin spiral with small q limit, Eq. (A5) can be written as

$$\lim_{q\to 0} \Delta E_{\mathrm{DM}}(\boldsymbol{q}) = \frac{\sqrt{3}}{2} dqa. \tag{A6}$$

We calculate the spin spiral energy dispersion within $|q| \leqslant 0.1(2\pi/a)$ and obtain d by linear fitting. For the term of magnetic anisotropy, we focus on three main magnetic states, i.e., magnetized along the normal direction $\boldsymbol{e}_{\mathrm{N}}$ (E_{N}), the tangential direction $\boldsymbol{e}_{\mathrm{T}}$ (E_{T}), and the binormal direction $\boldsymbol{e}_{\mathrm{B}}$ (E_{B}). The magnetic anisotropy K is calculated by $K = E_{\mathrm{N}} - \frac{1}{2}(E_{\mathrm{B}} + E_{\mathrm{T}})$.

The static spin profiles are calculated using the VAMPIRE package [75] by solving the atomistic Landau-Lifshitz-Gilbert equation given by

$$\frac{\partial \boldsymbol{S_i}}{\partial t} = -\frac{\gamma}{(1+\lambda^2)}[\boldsymbol{S_i} \times \boldsymbol{B_{\mathrm{eff}}} + \lambda \boldsymbol{S_i} \times (\boldsymbol{S_i} \times \boldsymbol{B_{\mathrm{eff}}})], \tag{A7}$$

which models the interaction of an atomic unit spin moment $\boldsymbol{S}_i$ with an effective magnetic field $\boldsymbol{B}_{\mathrm{eff}} = -1/\mu_s \partial\mathcal{H}/\partial\boldsymbol{S}_i$. The effective magnetic field is modeled using curvilinear spin Hamiltonian $\mathcal{H}$ given by Eq. (3). The gyromagnetic ratio γ and damping constant λ are set to be 1.76×10^{11} rad s^{-1} T^{-1} and 0.2. In the simulations, we reduce the magnetostatics to an effective easy-surface anisotropy, i.e., the effective magnetic anisotropy $K_{\mathrm{eff}} = K - \frac{1}{2}\mu_0 M_s^2$ directed towards the surface normal with μ_0 and M_s being the vacuum permeability and saturation magnetization. We also include the magnetostatic interactions and calculated magnetic anisotropy K in the atomistic Landau-Lifshitz-Gilbert simulations to find the ground states of folded systems. The relaxed spin textures of (N,π) folded CrI_3 are shown. It can be seen that the chiral domain states are robust in the folded systems with different spin Hamiltonian, indicating that the effective magnetic anisotropy K_{eff} is suitable for the considered folded CrI_3 systems.

APPENDIX B: FERT-LÉVY MODEL APPLIED TO THE DMI IN FOLDED $CrGeTe_3$ AND Fe_3GeTe_2

Similar to CrI_3, the three-site model can also be extended to the case of insulating $CrGeTe_3$ and metallic Fe_3GeTe_2 with local curvature. The three-site Fert-Lévy model has been widely used to explain the DMI mechanism in Cu:Mn dilute alloys with heavy metal impurities, at an interface between a magnetic metal and a nonmagnetic metal of large SOC, and in the 2D case [24,42]. In these cases, the DMI arising from electron exchange scattering on the two magnetic atoms and SOC scattering on a nonmagnetic atom with strong SOC. According to the previous theoretical studies [76,77], the spin model of Fe_3GeTe_2 can be adapted to a collective 2D model by treating three Fe layers of the Fe_3GeTe_2 as a whole. The calculated results have demonstrated that within this spin model, even in the case of metallic Fe_3GeTe_2, the exchange interaction remains relatively localized. Specifically, the nearest neighbors make the most significant

contributions to the exchange interaction. Thus, the three-site model can also be extended to the case of metallic Fe_3GeTe_2 with local curvature, with the Te atoms as the source of SOC. A similar situation can be found in $Fe_{3-\delta}GeTe_2$, where the out-of-plane displacement of the middle Fe causes Fert-Lévy DMI [78].

[1] R. Streubel, P. Fischer, F. Kronast, V. P. Kravchuk, D. D. Sheka, Y. Gaididei, O. G. Schmidt, and D. Makarov, Magnetism in curved geometries, J. Phys. D: Appl. Phys. **49**, 363001 (2016).

[2] C. K. Safeer, E. Jué, A. Lopez, L. Buda-Prejbeanu, S. Auffret, S. Pizzini, O. Boulle, I. M. Miron, and G. Gaudin, Spin–orbit torque magnetization switching controlled by geometry, Nat. Nanotechnol. **11**, 143 (2016).

[3] A. Fernández-Pacheco, R. Streubel, O. Fruchart, R. Hertel, P. Fischer, and R. P. Cowburn, Three-dimensional nanomagnetism, Nat. Commun. **8**, 15756 (2017).

[4] M. Z. Miskin, K. J. Dorsey, B. Bircan, Y. Han, D. A. Muller, P. L. McEuen, and I. Cohen, Graphene-based bimorphs for micron-sized, autonomous origami machines, Proc. Natl. Acad. Sci. USA **115**, 466 (2018).

[5] H. Chen, X.-L. Zhang, Y.-Y. Zhang, D. Wang, D.-L. Bao, Y. Que, W. Xiao, S. Du, M. Ouyang, S. T. Pantelides, and H.-J. Gao, Atomically precise, custom-design origami graphene nanostructures, Science **365**, 1036 (2019).

[6] C. Donnelly, S. Finizio, S. Gliga, M. Holler, A. Hrabec, M. Odstrčil, S. Mayr, V. Scagnoli, L. J. Heyderman, M. Guizar-Sicairos, and J. Raabe, Time-resolved imaging of three-dimensional nanoscale magnetization dynamics, Nat. Nanotechnol. **15**, 356 (2020).

[7] C. Donnelly, A. Hierro-Rodríguez, C. Abert, K. Witte, L. Skoric, D. Sanz-Hernández, S. Finizio, F. Meng, S. McVitie, J. Raabe, D. Suess, R. Cowburn, and A. Fernández-Pacheco, Complex free-space magnetic field textures induced by three-dimensional magnetic nanostructures, Nat. Nanotechnol. **17**, 136 (2022).

[8] A. Edstrom, D. Amoroso, S. Picozzi, P. Barone, and M. Stengel, Curved magnetism in CrI_3, Phys. Rev. Lett. **128**, 177202 (2022).

[9] M. Yan, A. Kákay, S. Gliga, and R. Hertel, Beating the Walker limit with massless domain walls in cylindrical nanowires, Phys. Rev. Lett. **104**, 057201 (2010).

[10] Y. Gaididei, V. P. Kravchuk, and D. D. Sheka, Curvature effects in thin magnetic shells, Phys. Rev. Lett. **112**, 257203 (2014).

[11] D. D. Sheka, V. P. Kravchuk, and Y. Gaididei, Curvature effects in statics and dynamics of low dimensional magnets, J. Phys. A: Math. Theor. **48**, 125202 (2015).

[12] V. P. Kravchuk, D. D. Sheka, A. Kakay, O. M. Volkov, U. K. Rossler, J. van den Brink, D. Makarov, and Y. Gaididei, Multiplet of skyrmion states on a curvilinear defect: Reconfigurable skyrmion lattices, Phys. Rev. Lett. **120**, 067201 (2018).

[13] Y. Zhang, J. Liu, Y. Dong, S. Wu, J. Zhang, J. Wang, J. Lu, A. Rückriegel, H. Wang, R. Duine, H. Yu, Z. Luo, K. Shen, and J. Zhang, Strain-driven Dzyaloshinskii-Moriya interaction for room-temperature magnetic skyrmions, Phys. Rev. Lett. **127**, 117204 (2021).

[14] O. M. Volkov, D. Wolf, O. V. Pylypovskyi, A. Kákay, D. D. Sheka, B. Buchner, J. Fassbender, A. Lubk, and D. Makarov, Chirality coupling in topological magnetic textures with multiple magnetochiral parameters, Nat. Commun. **14**, 1491 (2023).

[15] I. Dzyaloshinsky, A thermodynamic theory of "weak" ferromagnetism of antiferromagnetics, J. Phys. Chem. Solids **4**, 241 (1958).

[16] T. Moriya, Anisotropic superexchange interaction and weak ferromagnetism, Phys. Rev. **120**, 91 (1960).

[17] J. Sampaio, V. Cros, S. Rohart, A. Thiaville, and A. Fert, Nucleation, stability and current-induced motion of isolated magnetic skyrmions in nanostructures, Nat. Nanotechnol. **8**, 839 (2013).

[18] K. Litzius, I. Lemesh, B. Krüger, P. Bassirian, L. Caretta, K. Richter, F. Büttner, K. Sato, O. A. Tretiakov, J. Förster, R. M. Reeve, M. Weigand, I. Bykova, H. Stoll, G. Schütz, G. S. D. Beach, and M. Kläui, Skyrmion Hall effect revealed by direct time-resolved X-ray microscopy, Nat. Phys. **13**, 170 (2017).

[19] J. Barker and O. A. Tretiakov, Static and dynamical properties of antiferromagnetic skyrmions in the presence of applied current and temperature, Phys. Rev. Lett. **116**, 147203 (2016).

[20] A. Fert, N. Reyren, and V. Cros, Magnetic skyrmions: Advances in physics and potential applications, Nat. Rev. Mater. **2**, 17031 (2017).

[21] F. Hellman, A. Hoffmann, Y. Tserkovnyak, G. S. D. Beach, E. E. Fullerton, C. Leighton, A. H. MacDonald, D. C. Ralph, D. A. Arena, H. A. Dürr, P. Fischer, J. Grollier, J. P. Heremans, T. Jungwirth, A. V. Kimel, B. Koopmans, I. N. Krivorotov, S. J. May, A. K. Petford-Long, J. M. Rondinelli, N. Samarth, I. K. Schuller, A. N. Slavin, M. D. Stiles, O. Tchernyshyov, A. Thiaville, and B. L. Zink, Interface-induced phenomena in magnetism, Rev. Mod. Phys. **89**, 025006 (2017).

[22] J. Tang, Y. Wu, W. Wang, L. Kong, B. Lv, W. Wei, J. Zang, M. Tian, and H. Du, Magnetic skyrmion bundles and their current-driven dynamics, Nat. Nanotechnol. **16**, 1086 (2021).

[23] B. Göbel, I. Mertig, and O. A. Tretiakov, Beyond skyrmions: Review and perspectives of alternative magnetic quasiparticles, Phys. Rep. **895**, 1 (2021).

[24] A. Fert, M. Chshiev, A. Thiaville, and H. Yang, From early theories of Dzyaloshinskii–Moriya interactions in metallic systems to today's novel roads, J. Phys. Soc. Jpn. **92**, 081001 (2023).

[25] S. Mühlbauer, B. Binz, F. Jonietz, C. Pfleiderer, A. Rosch, A. Neubauer, R. Georgii, and P. Böni, Skyrmion lattice in a chiral magnet, Science **323**, 915 (2009).

[26] X. Yu, Y. Onose, N. Kanazawa, J. H. Park, J. Han, Y. Matsui, N. Nagaosa, and Y. Tokura, Real-space observation of a two-dimensional skyrmion crystal, Nature (London) **465**, 901 (2010).

[27] X. Yu, N. Kanazawa, Y. Onose, K. Kimoto, W. Zhang, S. Ishiwata, Y. Matsui, and Y. Tokura, Near room-temperature formation of a skyrmion crystal in thin-films of the helimagnet FeGe, Nat. Mater. **10**, 106 (2011).

[28] H. Du, R. Che, L. Kong, X. Zhao, C. Jin, C. Wang, J. Yang, W. Ning, R. Li, C. Jin, X. Chen, J. Zang, Y. Zhang, and M. Tian, Edge-mediated skyrmion chain and its collective dynamics in a confined geometry, Nat. Commun. **6**, 8504 (2015).

[29] F. Zheng, H. Li, S. Wang, D. Song, C. Jin, W. Wei, A. Kovács, J. Zang, M. Tian, Y. Zhang, H. Du, and R. E. Dunin-Borkowski,

Direct imaging of a zero-field target skyrmion and its polarity switch in a chiral magnetic nanodisk, Phys. Rev. Lett. **119**, 197205 (2017).

[30] F. Zheng, F. N. Rybakov, A. B. Borisov, D. Song, S. Wang, Z.-A. Li, H. Du, N. S. Kiselev, J. Caron, A. Kovács, M. Tian, Y. Zhang, S. Blügel, and R. E. Dunin-Borkowski, Experimental observation of chiral magnetic bobbers in B20-type FeGe, Nat. Nanotechnol. **13**, 451 (2018).

[31] S. Heinze, K. Von Bergmann, M. Menzel, J. Brede, A. Kubetzka, R. Wiesendanger, G. Bihlmayer, and S. Blügel, Spontaneous atomic-scale magnetic skyrmion lattice in two dimensions, Nat. Phys. **7**, 713 (2011).

[32] A. Thiaville, S. Rohart, É. Jué, V. Cros, and A. Fert, Dynamics of Dzyaloshinskii domain walls in ultrathin magnetic films, Europhys. Lett. **100**, 57002 (2012).

[33] O. Boulle, S. Rohart, L. D. Buda-Prejbeanu, E. Jue, I. M. Miron, S. Pizzini, J. Vogel, G. Gaudin, and A. Thiaville, Domain wall tilting in the presence of the Dzyaloshinskii-Moriya interaction in out-of-plane magnetized magnetic nanotracks, Phys. Rev. Lett. **111**, 217203 (2013).

[34] S. Rohart and A. Thiaville, Skyrmion confinement in ultrathin film nanostructures in the presence of Dzyaloshinskii-Moriya interaction, Phys. Rev. B **88**, 184422 (2013).

[35] H. Yang, A. Thiaville, S. Rohart, A. Fert, and M. Chshiev, Anatomy of Dzyaloshinskii-Moriya interaction at Co/Pt interfaces, Phys. Rev. Lett. **115**, 267210 (2015).

[36] O. Boulle, J. Vogel, H. Yang, S. Pizzini, D. de Souza Chaves, A. Locatelli, T. O. Menteş, A. Sala, L. D. Buda-Prejbeanu, O. Klein, M. Belmeguenai, Y. Roussigné, A. Stashkevich, S. M. Chérif, L. Aballe, M. Foerster, M. Chshiev, S. Auffret, I. M. Miron, and G. Gaudin, Room-temperature chiral magnetic skyrmions in ultrathin magnetic nanostructures, Nat. Nanotechnol. **11**, 449 (2016).

[37] S. Woo, K. Litzius, B. Krüger, M.-Y. Im, L. Caretta, K. Richter, M. Mann, A. Krone, R. M. Reeve, M. Weigand, P. Agrawal, I. Lemesh, M.-A. Mawass, P. Fischer, M. Kläui, and G. S. D. Beach, Observation of room-temperature magnetic skyrmions and their current-driven dynamics in ultrathin metallic ferromagnets, Nat. Mater. **15**, 501 (2016).

[38] T. H. Pham, J. Vogel, J. Sampaio, M. Vaňatka, J.-C. Rojas-Sánchez, M. Bonfim, D. S. Chaves, F. Choueikani, P. Ohresser, E. Otero, A. Thiaville, and S. Pizzini, Very large domain wall velocities in Pt/Co/GdO_x and Pt/Co/Gd trilayers with Dzyaloshinskii-Moriya interaction, Europhys. Lett. **113**, 67001 (2016).

[39] S. Tacchi, R. E. Troncoso, M. Ahlberg, G. Gubbiotti, M. Madami, J. Akerman, and P. Landeros, Interfacial Dzyaloshinskii-Moriya interaction in Pt/CoFeB films: Effect of the heavy-metal thickness, Phys. Rev. Lett. **118**, 147201 (2017).

[40] H. Yang, G. Chen, A. A. C. Cotta, A. T. N'Diaye, S. A. Nikolaev, E. A. Soares, W. A. A. Macedo, K. Liu, A. K. Schmid, A. Fert, and M. Chshiev, Significant Dzyaloshinskii–Moriya interaction at graphene–ferromagnet interfaces due to the Rashba effect, Nat. Mater. **17**, 605 (2018).

[41] J. Jiang, Z. Wang, J. Liang, Q. Cui, W. Mi, and H. Yang, Interfacial Dzyaloshinskii-Moriya interaction and perpendicular magnetic anisotropy at cobalt/diamond interfaces, J. Magn. Magn. Mater. **529**, 167852 (2021).

[42] H. Yang, J. Liang, and Q. Cui, First-principles calculations for Dzyaloshinskii–Moriya interaction, Nat. Rev. Phys. **5**, 43 (2022).

[43] J. Liang, W. Wang, H. Du, A. Hallal, K. Garcia, M. Chshiev, A. Fert, and H. Yang, Very large Dzyaloshinskii-Moriya interaction in two-dimensional Janus manganese dichalcogenides and its application to realize skyrmion states, Phys. Rev. B **101**, 184401 (2020).

[44] J. Jiang, X. Liu, R. Li, and W. Mi, Topological spin textures in a two-dimensional $MnBi_2(Se,\ Te)_4$ Janus material, Appl. Phys. Lett. **119**, 072401 (2021).

[45] J. Jiang, R. Li, and W. Mi, Electrical control of topological spin textures in two-dimensional multiferroics, Nanoscale **13**, 20609 (2021).

[46] Q. Cui, Y. Zhu, J. Jiang, J. Liang, D. Yu, P. Cui, and H. Yang, Ferroelectrically controlled topological magnetic phase in a Janus-magnet-based multiferroic heterostructure, Phys. Rev. Res. **3**, 043011 (2021).

[47] T.-E. Park, L. Peng, J. Liang, A. Hallal, F. S. Yasin, X. Zhang, K. M. Song, S. J. Kim, K. Kim, M. Weigand, G. Schütz, S. Finizio, J. Raabe, K. Garcia, J. Xia, Y. Zhou, M. Ezawa, X. Liu, J. Chang, H. C. Koo, Y. D. Kim, M. Chshiev, A. Fert, H. Yang, X. Yu, and S. Woo, Néel-type skyrmions and their current-induced motion in van der Waals ferromagnet-based heterostructures, Phys. Rev. B **103**, 104410 (2021).

[48] Y. Ga, Q. Cui, J. Liang, D. Yu, Y. Zhu, L. Wang, and H. Yang, Dzyaloshinskii-Moriya interaction and magnetic skyrmions induced by curvature, Phys. Rev. B **106**, 054426 (2022).

[49] Y. Ga, Q. Cui, Y. Zhu, D. Yu, L. Wang, J. Liang, and H. Yang, Anisotropic Dzyaloshinskii-Moriya interaction protected by D_{2d} crystal symmetry in two-dimensional ternary compounds, npj Comput. Mater. **8**, 128 (2022).

[50] R. Hertel, Curvature-induced magnetochirality, Spin **3**, 1340009 (2013).

[51] D. D. Sheka, O. V. Pylypovskyi, P. Landeros, Y. Gaididei, A. Kákay, and D. Makarov, Nonlocal chiral symmetry breaking in curvilinear magnetic shells, Commun. Phys. **3**, 128 (2020).

[52] K. Yershov, V. Kravchuk, D. Sheka, and U. Roessler, Curvature effects on phase transitions in chiral magnets, SciPost Phys. **9**, 043 (2020).

[53] A. Fasolino, J. Los, and M. I. Katsnelson, Intrinsic ripples in graphene, Nat. Mater. **6**, 858 (2007).

[54] B. Huang, G. Clark, E. Navarro-Moratalla, D. R. Klein, R. Cheng, K. L. Seyler, D. Zhong, E. Schmidgall, M. A. McGuire, D. H. Cobden, W. Yao, D. Xiao, P. Jarillo-Herrero, and X. Xu, Layer-dependent ferromagnetism in a van der Waals crystal down to the monolayer limit, Nature (London) **546**, 270 (2017).

[55] C. Gong, L. Li, Z. Li, H. Ji, A. Stern, Y. Xia, T. Cao, W. Bao, C. Wang, Y. Wang, Z. Q. Qiu, R. J. Cava, S. G. Louie, J. Xia, and X. Zhang, Discovery of intrinsic ferromagnetism in two-dimensional van der Waals crystals, Nature (London) **546**, 265 (2017).

[56] Y. Deng, Y. Yu, Y. Song, J. Zhang, N. Z. Wang, Z. Sun, Y. Yi, Y. Z. Wu, S. Wu, J. Zhu, J. Wang, X. H. Chen, and Y. Zhang, Gate-tunable room-temperature ferromagnetism in two-dimensional Fe_3GeTe_2, Nature (London) **563**, 94 (2018).

[57] H. K. Ng, D. Xiang, A. Suwardi, G. Hu, K. Yang, Y. Zhao, T. Liu, Z. Cao, H. Liu, S. Li, J. Cao, Q. Zhu, Z. Dong, C. K. I. Tan, D. Chi, C.-W. Qiu, K. Hippalgaonkar, G. Eda, M. Yang, and J. Wu, Improving carrier mobility in two-dimensional

semiconductors with rippled materials, Nat. Electron. **5**, 489 (2022).
[58] R. R. Birss, *Symmetry and Magnetism* (North-Holland, Amsterdam, 1966).
[59] A. Di Pietro, P. Ansalone, V. Basso, A. Magni, and G. Durin, Gauge theory applied to magnetic lattices, Europhys. Lett. **140**, 46003 (2022).
[60] S. Jiang, L. Li, Z. Wang, K. F. Mak, and J. Shan, Controlling magnetism in 2D CrI_3 by electrostatic doping, Nat. Nanotechnol. **13**, 549 (2018).
[61] Z. Wang, I. Gutiérrez-Lezama, N. Ubrig, M. Kroner, M. Gibertini, T. Taniguchi, K. Watanabe, A. Imamoğlu, E. Giannini, and A. F. Morpurgo, Very large tunneling magnetoresistance in layered magnetic semiconductor CrI_3, Nat. Commun. **9**, 2516 (2018).
[62] S. Kumar and P. Suryanarayana, Bending moduli for forty-four select atomic monolayers from first principles, Nanotechnology **31**, 43LT01 (2020).
[63] J. L. Lado and J. Fernández-Rossier, On the origin of magnetic anisotropy in two dimensional CrI_3, 2D Mater. **4**, 035002 (2017).
[64] A. Fert and P. M. Levy, Role of anisotropic exchange interactions in determining the properties of spin-glasses, Phys. Rev. Lett. **44**, 1538 (1980).
[65] G. Qiu, Z. Li, K. Zhou, and Y. Cai, Flexomagnetic noncollinear state with a plumb line shape spin configuration in edged two-dimensional magnetic CrI_3, npj Quantum Mater. **8**, 15 (2023).
[66] G. Kresse and J. Hafner, *Ab initio* molecular dynamics for liquid metals, Phys. Rev. B **47**, 558 (1993).
[67] G. Kresse and J. Hafner, *Ab initio* molecular-dynamics simulation of the liquid-metal–amorphous-semiconductor transition in germanium, Phys. Rev. B **49**, 14251 (1994).
[68] G. Kresse and J. Furthmüller, Efficiency of ab-initio total energy calculations for metals and semiconductors using a plane-wave basis set, Comput. Mater. Sci. **6**, 15 (1996).
[69] G. Kresse and J. Furthmüller, Efficient iterative schemes for *ab initio* total-energy calculations using a plane-wave basis set, Phys. Rev. B **54**, 11169 (1996).
[70] J. P. Perdew, K. Burke, and M. Ernzerhof, Generalized gradient approximation made simple, Phys. Rev. Lett. **77**, 3865 (1996).
[71] S. L. Dudarev, G. A. Botton, S. Y. Savrasov, C. Humphreys, and A. P. Sutton, Electron-energy-loss spectra and the structural stability of nickel oxide: An LSDA+U study, Phys. Rev. B **57**, 1505 (1998).
[72] A. Kartsev, M. Augustin, R. F. L. Evans, K. S. Novoselov, and E. J. G. Santos, Biquadratic exchange interactions in two-dimensional magnets, npj Comput. Mater. **6**, 150 (2020).
[73] L. M. Sandratskii, Insight into the Dzyaloshinskii-Moriya interaction through first-principles study of chiral magnetic structures, Phys. Rev. B **96**, 024450 (2017).
[74] J. Liang, Q. Cui, and H. Yang, Electrically switchable Rashba-type Dzyaloshinskii-Moriya interaction and skyrmion in two-dimensional magnetoelectric multiferroics, Phys. Rev. B **102**, 220409 (2020).
[75] R. F. Evans, W. J. Fan, P. Chureemart, T. A. Ostler, M. O. Ellis, and R. W. Chantrell, Atomistic spin model simulations of magnetic nanomaterials, J. Phys.: Condens. Matter **26**, 103202 (2014).
[76] D. Li, S. Haldar, and S. Heinze, Strain-driven zero-field near-10 nm skyrmions in two-dimensional van der Waals heterostructures, Nano Lett. **22**, 7706 (2022).
[77] D. Li, S. Haldar, T. Drevelow, and S. Heinze, Tuning the magnetic interactions in van der Waals Fe_3GeTe_2 heterostructures: A comparative study of *ab initio* methods, Phys. Rev. B **107**, 104428 (2023).
[78] C. Liu, J. Jiang, C. Zhang, Q. Wang, H. Zhang, D. Zheng, Y. Li, Y. Ma, H. Algaidi, X. Gao, Z. Hou, W. Mi, J.-M. Liu, Z. Qiu, and X. Zhang, Controllable skyrmionic phase transition between Néel skyrmions and Bloch skyrmionic bubbles in van der Waals ferromagnet $Fe_{3-\delta}GeTe_2$, Adv. Sci. **10**, 2303443 (2023).